Original Article

Institution of MECHANICAL ENGINEERS

Journal of ENGINEERING FOR THE MARITIME ENVIRONMENT

Proc IMechE Part M:
J Engineering for the Maritime Environment
1–13

DOI: 10.1177/1475090219863191
journals.sagepub.com/home/pim
SAGE

Optimal design of nose and tail of an autonomous underwater vehicle hull to reduce drag force using numerical simulation

Mohammad Saghafi[1] and Roham Lavimi[2]

Abstract

In this research, the flow around the autonomous underwater vehicles with symmetrical bodies is numerically investigated. Increasing the drag force in autonomous underwater vehicles increases the energy consumption and decreases the duration of underwater exploration and operations. Therefore, the main objective of this research is to decrease drag force with the change in geometry to reduce energy consumption. In this study, the decreasing or increasing trends of the drag force of axisymmetric bare hulls have been studied by making alterations in the curve equations and creating the optimal geometric shapes in terms of hydrodynamics for the noses and tails of autonomous underwater vehicles. The incompressible, three-dimensional, and steady Navier–Stokes equations have been used to simulate the flow. Also, k-ε Realizable with enhanced wall treatment was used for turbulence modeling. Validation results were acceptable with respect to the 3.6% and 1.4% difference with numerical and experimental results. The results showed that all the autonomous underwater vehicle hulls designed in this study, at an attack angle of 0°, had a lower drag force than the autonomous underwater vehicle hull used for validation except geometry no. 1. In addition, nose no. 3 has been selected as the best nose according to the lowest value of stagnation pressure, and also tail no. 3 has been chosen as the best tail due to the production of the lowest vortex. Therefore, geometry no. 5 has been designed using nose and tail no. 3. The comparison made here showed that the maximum drag reduction in geometry no. 5 was equal to 26%, and therefore, it has been selected as the best bare hull in terms of hydrodynamics.

Keywords

Autonomous underwater vehicle hull, optimal nose, optimal tail, computational fluid dynamics, drag estimation

Date received: 4 February 2019; accepted: 19 June 2019

Introduction

Autonomous underwater vehicles (AUVs) are increasingly popular for ocean exploration and industrial applications. This type of underwater vehicles has recently become an attractive alternative for underwater search and exploration since they are cheaper than manned vehicles. Over the past years, there have been abundant attempts to develop underwater vehicles to meet the challenge of exploration and extraction programs in the oceans. Recently, researchers have focused on the development of AUVs for long-term data collection in oceanography and coastal management.[1]

The growth of collaborative activities of AUVs has increased the importance of optimizing their energy consumption.[2] Operation of these underwater vehicles is often faced with the limited capacity of energy storage. The energy sources of this kind of vehicles mainly consist of batteries and fuel cells. Underwater vehicles must store energy while monitoring so that they can travel longer distances over a period of time. There are several ways to do this: first, upgrading the existing batteries to their newer type, that is, lithium-ion, second, the use of more efficient motors and lower energy consumption, and the third alternative is to change the geometry of underwater vehicles and to streamline them as much as possible. This means to consider a less resistant

[1]Department of Mechanical Engineering, West Tehran Branch, Islamic Azad University, Tehran, Iran
[2]Young Researchers and Elite Club, Khorramabad Branch, Islamic Azad University, Khorramabad, Iran

Corresponding author:
Roham Lavimi, Young Researchers and Elite Club, Khorramabad Branch, Islamic Azad University, Khorramabad 68816, Iran.
Email: roham.lavimi@smc.iaun.ac.ir; rlavimi@yahoo.com

body shape.[3] Hence, in the early stage of designing AUVs, the reduction of body resistance is one of the key objectives of design.[4] So far, many numerical studies have been conducted to calculate drag of underwater vehicles. Karim et al.[5] have numerically quantified viscose drag using a finite-volume method based on the Reynolds-averaged Navier–Stokes equations on DREA submarine hull and six axisymmetric bodies. Payne[6] has provided an approach to calculate the drag of axisymmetric bodies. The results indicated that the optimization method is distinct from any particular drag model so that the effects of minimum-drag bodies can be investigated by replacing the models.

In addition, a method to estimate hydrodynamic coefficients of an AUV with non-aerodynamic geometry (TUNA-SAND) has been studied.[7] The results showed that the use of numerical methods not only allows for the determination of linear and nonlinear coefficients but also the results of this type of simulation are not limited to small movement areas of vehicles. Findings of a study by Sarkar et al.[8] showed that the standard wall functions turbulence model can calculate the flow specifications with at least an accuracy equal to that of Chen–Kim modified k–ε model and renormalization group (RNG). Four axisymmetric bare hulls, including AFTERBODY 1, AFTERBODY 2 of DTNSRDC, modified spheroid (MS), and F-57 were utilized in the aforementioned work.

So far, attempts have been made to study the reduction of drag on the various bare hulls. Shereena[9] proposed a computational fluid dynamics (CFD) guideline to study the reduction of drag in axisymmetric underwater bodies by air jet injection in the boundary layer. In addition, De Sousa and de Macêdo[10] analyzed the turbulent single-phase fluid flow around the different bare hulls with different dimensions to experimentally identify the geometry which produces less drag force. The schematic shape of these geometries is inspired by the famous Myring hull shape. Moreover, Joung et al.[11] described a CFD approach to determine the resistance of the hull of a developing AUV for the given speed to rotate the propeller and the various speeds given for the AUV.

So far, studies have been performed to optimize the bare hulls using the multi-island genetic algorithm and particle swarm optimization.[12,13] Jagadeesh et al.[14] empirically proposed the forces and body momentum of an AUV on a vertical plate based on a towing tank. In their research, the shape of the given underwater vehicle was a model of AFTERBODY 1. The result of this test showed that these results can provide a better idea to design the guidance and system control for an AUV properly. The performance of elliptical cone shapes designed and developed to improve the hydrodynamic performance of an AUV has been studied.[15] The shape of the nose of an AUV has been studied by evaluating the performance of various profiles through computational analysis. This makes it clear that the hydrodynamic performance of the vehicle can be improved by having an elliptical cone profile. The designed vehicle having elliptical noses has been tested to evaluate the numerical results.

Many numerical studies have been carried out to simulate the flow around the AUVs with a variety of methods.[16–18] The nature of complex vertical flow structures around the axisymmetric body with two different nose shapes (SUBOFF and DRDC STR) was experimentally investigated. Results indicated the nose curvature effects on the separation position, and also nose separation for the model with blunter nose shape takes place in smaller incidence angles.[19] Saeidinezhad et al.[20] examined the behavior of a submarine model with a non-axisymmetric nose in pitch maneuver. The submarine model with all its appendages was tested with pitch angles between -10 and $+27$. It was shown that increasing the pitch angle results in a steady growth of lift and drag coefficients. In addition, cross-flow vortex structures over a submarine with the SUBOFF bow in comparison with a submarine with the DRDC STR bow was numerically and empirically conducted. According to the results, a submarine with DRDC STR bow generates larger lift and drag forces than another submarine.[21] Besides, surface pressure distributions were quantified over two kinds of nose shapes in different Reynolds numbers and pitch angles. Results revealed that variations of Reynolds number do not have a significant impact upon the nose surface pressure distribution at different pitch angles.[22] Zhang et al.[23] used a numerical code to simulate the viscous fluid flow around two models of underwater vehicles. The theory governing this code was derived from equations called FW-H. This numerical method was based on the large eddy simulation (LES) turbulence model and was used to predict the flow field, the wall-pressure distribution, and the flow analysis when hitting the nose. In addition, Liu et al.[24] calculated the flow around a rotating shape with electromagnetic controlled appendages to determine the effect of appendages on the flow and the effect of controlling electromagnetic force by a finite-volume method. The results suggested that elliptical appendages represent a complex wake structure and force fluctuation. Lorentz force may suppress the near-wall separation from the appendages and particularly may reduce the drag and vibration.

One of the ways to reduce energy consumption is to optimize the geometry of AUVs. Hydrodynamic optimization has rarely been applied to design AUVs since the existing design tools are not powerful or quick enough to be used in an optimization design. For this reason, former attempts to design previously reported AUVs have primarily been based on applied and non-optimal designs, which are often accepted as an adapted option. For instance, Stevenson et al.[25] recognized that there have been limitations to design AUVs. These limitations have caused the drag force to be underpredicted. Recent studies on the optimization of the AUV hull are often limited to the use of the formulas obtained in previous studies and the changes in their coefficients as well as the increase and decrease in some

of their factors, and more prominently they are not innovative. Since the noses and tails are among the most important sections of AUVs when hitting fluids, by optimizing these sections, drag force can be reduced by controlling the boundary layer, reducing the turbulent flow, and even preventing the formation of turbulent flow in the boundary layer.

This research has provided new work in this area using previous knowledge and the use of powerful software with alterations in various geometries in a way that the conditions of the problem are met. Due to the fact that the nose drag does not have any effect on the tail drag (due to the constant speed of the bare hull), it is permissible to use any noses on a body with a variety of tails. Therefore, after assuring the accuracy of the results obtained from the numerical solution, by making changes in the geometry of noses and tails in other underwater vehicles, many geometries are resulted, from among which, three noses are selected along with three tails, and then they are examined. Finally, the best axisymmetric bare hull is introduced with the least drag force produced.

Governing equations and numerical method

The incompressible, three-dimensional (3D) steady forms of governing equations are used for modeling the flow. Equations (1) and (2) are as follows:

Continuity equation

$$\frac{\partial v_i}{\partial x_i} = 0 \tag{1}$$

Momentum equation

$$\frac{\partial \rho v_i}{\partial t} + u_i \frac{\partial \rho v_i}{\partial x_j} = -\frac{\partial p}{\partial x_i} + \frac{\partial \tau_{ij}}{\partial x_i} + F_i \tag{2}$$

where x_i ($i = 1, 2, 3$) is the axes of the orthogonal coordinate system, v_i is the component of the fluid velocity vector, ρ is the water density, p is the pressure, τ_{ij} is the viscosity stress tensor of water, and F_i is the external force along x_i.

Numerical analysis on AUVs in low Reynolds showed that using k-ω Realizable, compared to the experimental results, shows better results.[26] Therefore, in the current study, k-ω Realizable with enhanced wall treatment is used for solving the required problems. k-ω Realizable model can precisely predict the spreading rate of both planar and round jets. Besides, it gives better performance for rotational flows, boundary layers under strong adverse pressure gradients, separation, and recirculation.[27]

Transport equations for the Realizable k-ω model:

$$\frac{\partial}{\partial t}(\rho k) + \frac{\partial}{\partial x_j}(\rho k u_j) = \frac{\partial}{\partial x_j}\left[\left(\mu + \frac{\mu_t}{\sigma_k}\right)\frac{\partial k}{\partial x_j}\right] + G_k + G_b - \rho\varepsilon - Y_M + S_k \tag{3}$$

$$\frac{\partial}{\partial t}(\rho \varepsilon) + \frac{\partial}{\partial x_j}(\rho \varepsilon u_j) = \frac{\partial}{\partial x_j}\left[\left(\mu + \frac{\mu_t}{\sigma_\epsilon}\right)\frac{\partial \varepsilon}{\partial x_j}\right] + \rho C_1 S\varepsilon - \rho C_2 \frac{\varepsilon^2}{k + \sqrt{\nu\varepsilon}} + C_{1\varepsilon}\frac{\varepsilon}{k} C_{3\varepsilon} G_b + S_\varepsilon \tag{4}$$

where $C_1 = [0.43,\ (\eta/(\eta + 5))],\ \eta = k/\varepsilon,\ S = \sqrt{2S_{ij}S_{ij}}$

In aforementioned equations, G_k is the generation of turbulence kinetic energy due to the mean velocity gradients, G_b is the generation of turbulence kinetic energy due to buoyancy, Y_M is the overall dissipation rate due to the fluctuating dilatation, C_2 and $C_{1\varepsilon}$ are constants, σ_k and σ_ϵ are the turbulent Prandtl numbers for k and ε, respectively. S_k and S_ε are user-defined source terms.[27]

In this study, ANSYS FLUENT software is utilized to solve the steady incompressible Navier–Stokes equations. The solver based on pressure and SIMPLE algorithms is used for the pressure–velocity coupling. Moreover, least squares cell-based, second-order, second-order upwind, and second-order upwind are used respectively, for the discretion of gradient, pressure, momentum, turbulent kinetic energy and specific dissipation rate, respectively. For computational domain, water density, viscosity, and PVC density used for body are considered 998.2 kg/m^3, 0.01003 kg/ms, and 2719 kg/m^3, respectively.

Geometric specifications and boundary conditions

Nose geometries

The sharp geometries in the nose section are not suitable due to the creation of a high-pressure gradient. The nose geometries used in this research are as follows. The Myring hull profile equation is as follows

$$r(x) = \frac{1}{2} d\left[1 - \left(\frac{x - a}{a}\right)^2\right]^{\frac{1}{n}} \tag{5}$$

Equation (5) is the modified semi-elliptical radius distribution,[28] where a is the length of the nose and d is the diameter of the cylinder and n is a variable coefficient that by changing it, the curve shape also changes, and x is the location of nose tip. By putting the constant value of $n = 2$ in equation (5), a two-dimensional (2D) shape is obtained that by rotating it around the Z axis, Figure 1 is resulted. In addition, the variables of the formula have been modified in such a way that the length of the nose becomes 250 mm and the radius of the nose becomes 125 mm.

By increasing the length of the curve, the shape of the object is streamlined and the decrease of drag around the body becomes more sensible. For this purpose, by increasing the nose length from 250 to 312 mm, and changing n to 7.7 and assuming a radius of 125 mm in equation (5), a 2D shape is obtained that by rotating it around the Z axis, a 3D shape is obtained (Figure 2). Since the drag coefficient changes with any

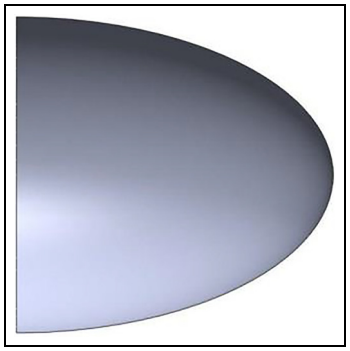

Figure 1. Nose no. 1.

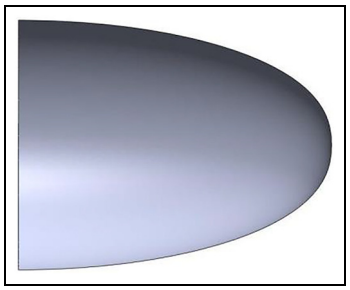

Figure 2. Nose no. 2.

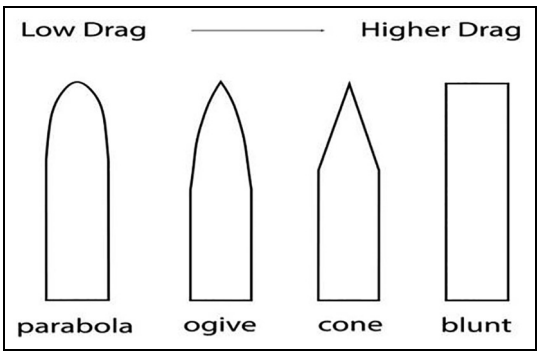

Figure 3. The alteration of drag coefficient in various object geometries.

alterations in nose type (Figure 3), as the curve becomes parabolic, the drag decreases.

The power series has a shape which is very similar to the parabolic nose. This series is known by its blunt nose. The 3D geometry of this type of nose is obtained by rotation of equation (6) around the X axis.

$$y = R\left(\frac{x}{L}\right)^n \tag{6}$$

where R is the radius of the nose and L is the length of the nose curve and n is a variable between 0 and 1. The suitable n for a nose is assumed to be 0.5. The 3D shape with a length of 400 mm and a radius of 125 mm is resulted from the rotation of the 2D shape around the Z axis (Figure 4). Figure 5 represents the geometry of the nose used by Khairul Alam et al.[26]

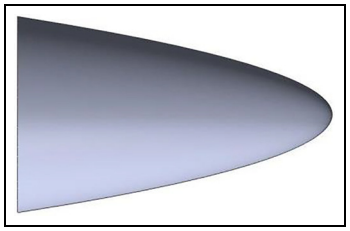

Figure 4. Nose no. 3.

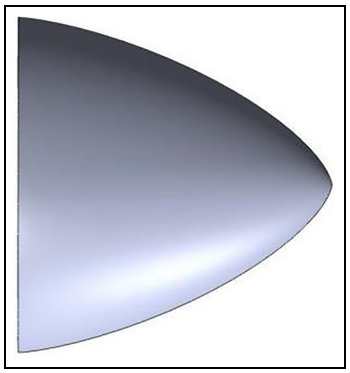

Figure 5. Nose was used by Alam et al.[26]

Tail geometries

Geometries with high bows are not suitable for tails of underwater vehicles due to the formation of vortices in the rear section, since the more smooth the deviation of flow is, the later the separation occurs on the tail. The geometry of the tail used by Alam et al.[26] is 312 mm in length (Figure 6).

An important profile, called tangent ogive, has been investigated in many studies, which is used both for the nose and tail. Figure 7 shows the tangent ogive schematic. R is the radius of the main curve, L is the length of the nose or tail, D is the total diameter of the nose or tail, and T is the diameter of the end section for the tail or the initial section for the nose. The curvature radius of this geometry is obtained from equation (7). Here, L is assumed to be 300 mm, D is considered as 250 mm and T is assumed to be 30 mm. Figure 8 has been formed by rotating it around the Z axis.

$$R = \frac{L^2}{D-T} + \frac{D-T}{4} \tag{7}$$

The second geometry for the tail of AUV is a special type of the Myring family derived from the formulas obtained by DF Myring.[28] Equation (8) is a tail curve in which a is the length of the nose, d is the diameter of the cylinder, b is the length of the cylinder part of the body, and θ is half of the tail angle in radian.

Myring[28] has studied three types of geometries with three different angles. In this article, the geometry with a 25° angle is selected by making variations in tail size and tail diameter.

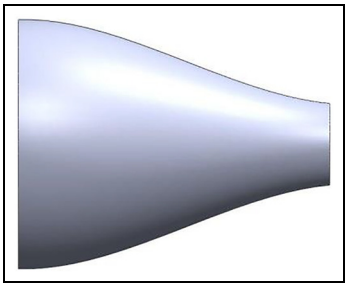

Figure 6. Tail was used by Alam et al.[26]

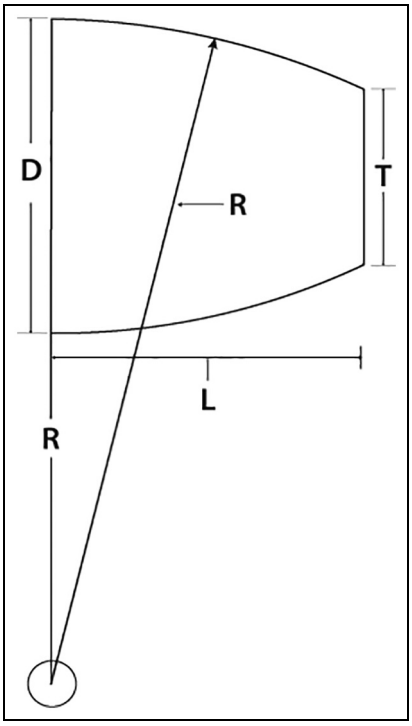

Figure 7. Tangent ogive schematic.

$$r = \frac{1}{2}d - \left\{\frac{3d}{2(100-a-b)^2} - \frac{\tan\theta}{(100-a-b)}\right\} \{x-a-b\}^2 + \left\{\frac{d}{(100-a-b)^3} - \frac{\tan\theta}{(100-a-b)^2}\right\} \{x-a-b\}^3 \quad (8)$$

By choosing the 25° angle for the equation and a change in the overall length from 100 to 130 mm, with a diameter of 250 mm and the tail length of 448.38 mm, a new 2D geometry is created that by rotating it around the Z axis, the 3D shape is obtained (Figure 9).

The profile of tail no. 3 has been drawn using equation (8) and by changing the curve length to 500 mm. Figure 10 shows a 3D schematic representation of this profile.

A group of body geometries has been studied in the current research, whose total length does not exceed

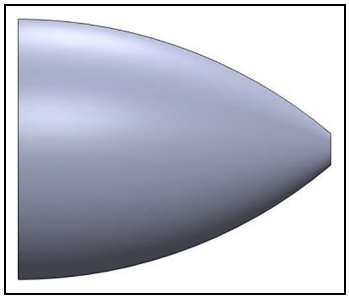

Figure 8. Tail no. 1.

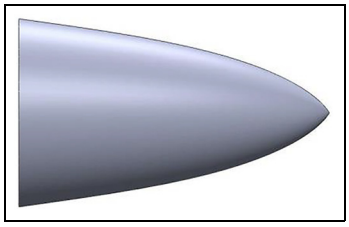

Figure 9. Tail no. 2.

1300 mm, their nose length does not go beyond 400 mm, and their tail length is at most 500 mm. In the present research, in order to prevent replication and repetition of previous work, simple geometries of the noses and tails are avoided applying, and the modified geometries are entirely investigated. By combining the provided noses and tails, four axisymmetric bare hulls are considered and numerically analyzed (Figure 11).

Boundary condition

Given the fact that the AUV hull shape is cylindrical, for better distribution of the mesh across the entire flow field, the solution domain is assumed to be cylindrical so that it matches the body geometry in terms of meshing and also to improve the accuracy of the analyses. In addition, since all the shapes are axisymmetric, the quarter model of the bare hull is considered for CFD analysis to reduce the computational costs. The dimensions of the computational domain and the boundary conditions are shown in Figure 12.

The problem-solving domain is 16 l from the upstream (front of the nose), 18 l from the downstream (behind the tail) and 10l around the cylinder surface which has a cylindrical shape; also, the boundary conditions of the problem have been set according to the sizes mentioned previously.[26]

The inlet boundary condition has been considered based on the constant speed condition (2 m/s) with turbulence intensity of 5% and a turbulent viscosity ratio of 10.[26] In addition, the outlet boundary condition has a static pressure condition. Due to the fact that the side walls are sufficiently distanced from the AUV hull, the effects of the flow in these areas on the AUV hull are negligible, and therefore, the side walls have a free slip

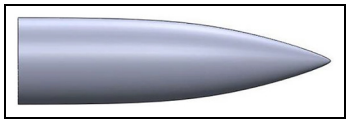

Figure 10. Tail no. 3.

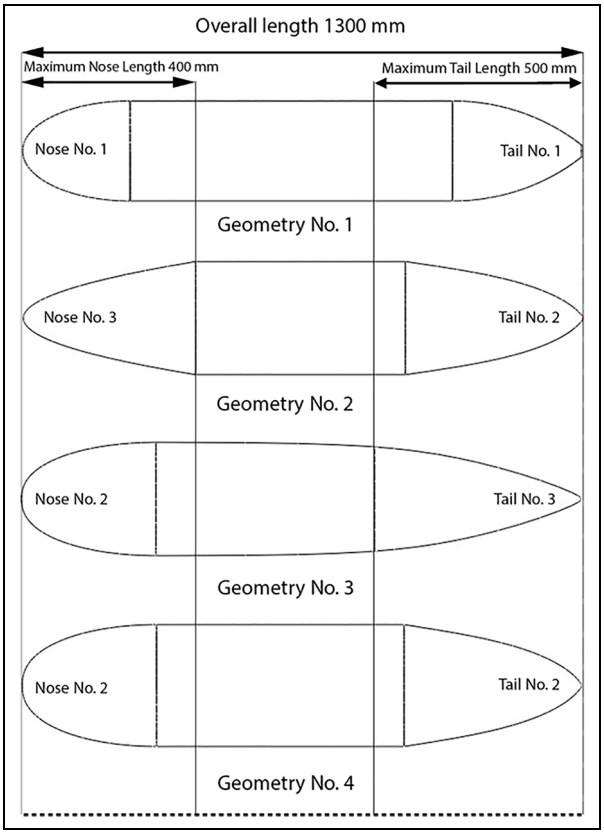

Figure 11. Geometry of AUV hull shapes.

condition. The no-slip condition is also considered as the boundary condition of the AUV hull.

Result and discussion

Validation and grid resolution test

In this research, the grid is unstructured, and in the regions such as the tail and rear of the vehicle, which have higher gradients, the number of mesh cells is increased; moreover, to increase the accuracy of the results, the boundary layer has been utilized around the body.[29] In order to achieve accurate numerical results, it has been attempted to lay the y^+ around the body in a range of 30–100 due to choosing k-ε Realizable with enhanced wall treatment.[26] Using equation (9), the thickness of the first layer is about 0.00157973 mm. In addition, 21 layers with the growth rate of 1.1 were utilized.

$$\Delta y = L\Delta y^+ \sqrt{80}\mathrm{Re}^{-\frac{13}{14}} \tag{9}$$

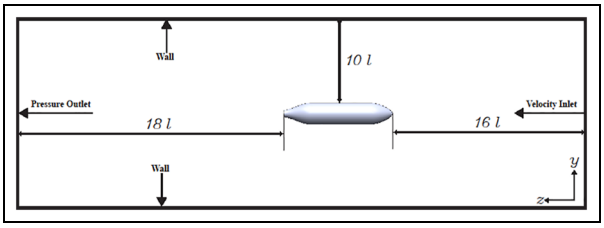

Figure 12. The size of computational domain boundary conditions.

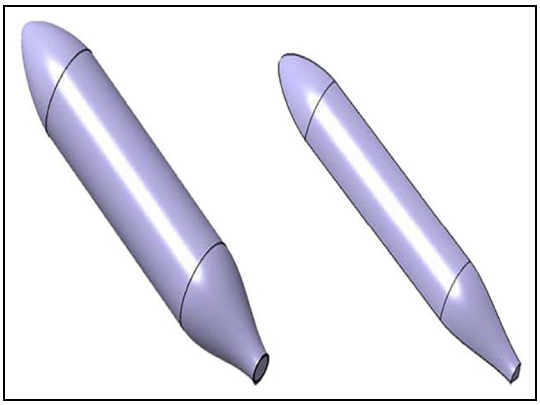

Figure 13. The AUV hull shape was designed by Alam et al.[26]

The data in Alam et al.'s[26] study which have experimentally and numerically dealt with design and the fabrication of AUV hull were used for validation of the present results. Figures 13 and 14 show an AUV designed by Alam et al. as well as the meshing around it.

In numerical simulations, the created grid is broken down to various stages for the numerical solution of the mesh to become independent. To do this, four different meshing sizes have been used. The results of Table 1 indicate that by increasing the number of mesh cells around the AUV hull used for validation, the drag force of fine and very fine meshes do not significantly change. Therefore, it has been tried to use the cell numbers of fine mesh for other simulation (782,438 cells). Table 2 shows the comparison of drag force with the data in Alam et al.'s study. As it is seen, the drag force obtained in this study (fine mesh with 782,438 cells) is 3.6% more than the numerical results and 1.4% more than the experimental results obtained by Alam et al. According to Figure 15, it is seen that the y^+ range of geometries is between 30 and 100, which is quite suitable for the k-ε Realizable with enhanced wall treatment turbulence model.[26]

Analysis of numerical results of AUVs designed

The lift and drag coefficients are defined as follows:

$$C_D = \frac{F_D}{\frac{1}{2}U_\infty^2 S} \tag{10}$$

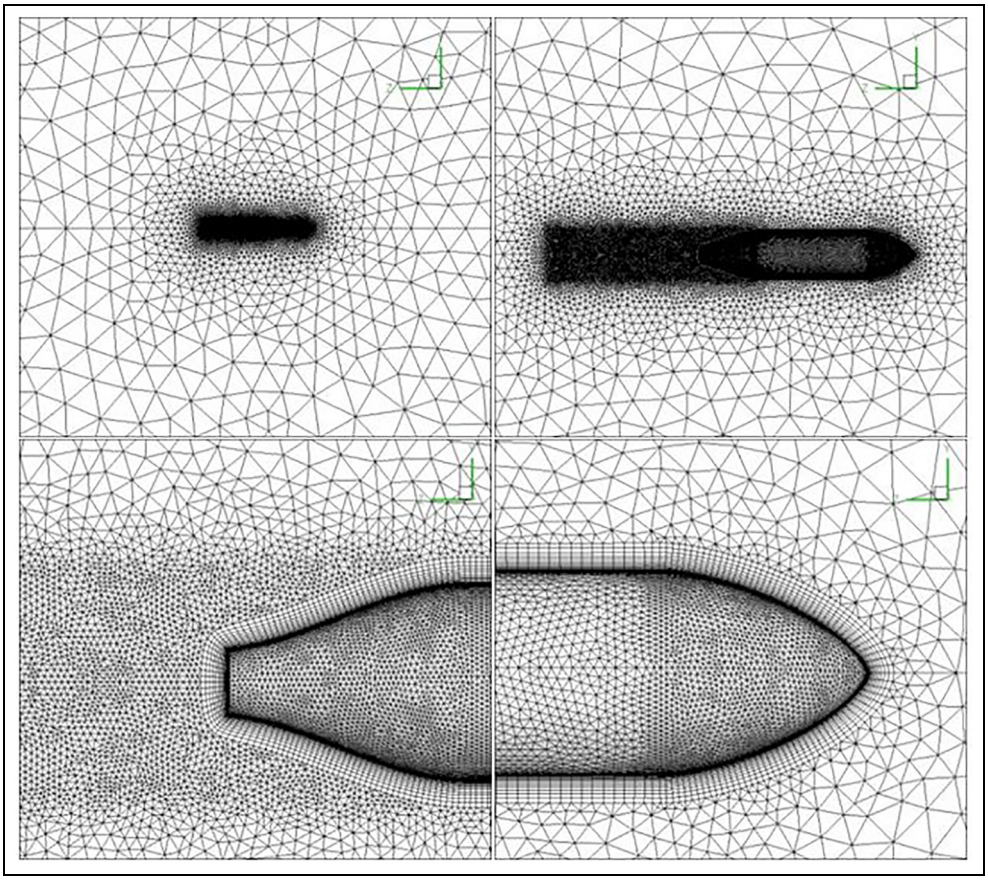

Figure 14. Grid generation around an AUV hull designed by Alam et al.

Table 1. Information of four grids used in this study.

Mesh density	No(s) of elements	Drag (N)
Coarse	381,236	11.75103
Medium	588,726	10.76239
Fine	782,438	9.79924
Very fine	978,051	9.65775

Table 2. The comparison between drag force in this research and that of Alam et al.[26]

	Numerical analysis	Experimental analysis
Alam et al.	9.44751 (N)	9.661129 (N)
Present study	9.79924 (N)	–

$$C_L = \frac{F_L}{\frac{1}{2}U_\infty^2 A} \tag{11}$$

where U_∞ is the reference speed, S is the front surface of the vehicle illustrated and A is the surface area of the body surface of the vehicle. Table 3 shows the lift and drag coefficients of different geometries. Figure 16 shows the pressure distribution around different AUV hulls. The flow accelerates when passing over bows, so pressure coefficients decrease rapidly. As it can be seen, the nose of geometry no. 2 has the highest curvature; thus, it leads to acceleration of the flow as much as possible, and eventually results in a sharp decrease in the pressure coefficient (approximately -0.5). However, the nose curvature used in geometries no. 3 and no. 4 (both having nose no. 2) has a very gentle slope that leads to minimal reduction in pressure coefficient. After increasing, the pressure gets close to the level of the free stream pressure and remains unchanged in the middle part of the AUVs. Although the onset of the flow separation leads to the reduction of the pressure coefficients again, the low velocity of the flow behind the stern parts increases of pressure increases of pressure coefficients. As it is seen, noses used in geometries no. 1, no. 2, and no. 4 has the highest curvature; therefore, a sharp drop in these shapes is clearly seen, while in geometry no. 3, due to the presence of a tail with low curvature, no significant decrease or increase in the pressure coefficient is observed, indicating that the separation is delayed.

Figure 17 shows streamline plots around the tail of the various AUV hulls. The reversed flow, which indicates the separation of the flow, is visible on the tail of geometries no. 1, no. 2, and no. 4, while the reversed flow is not seen on the tail of geometry no. 3.

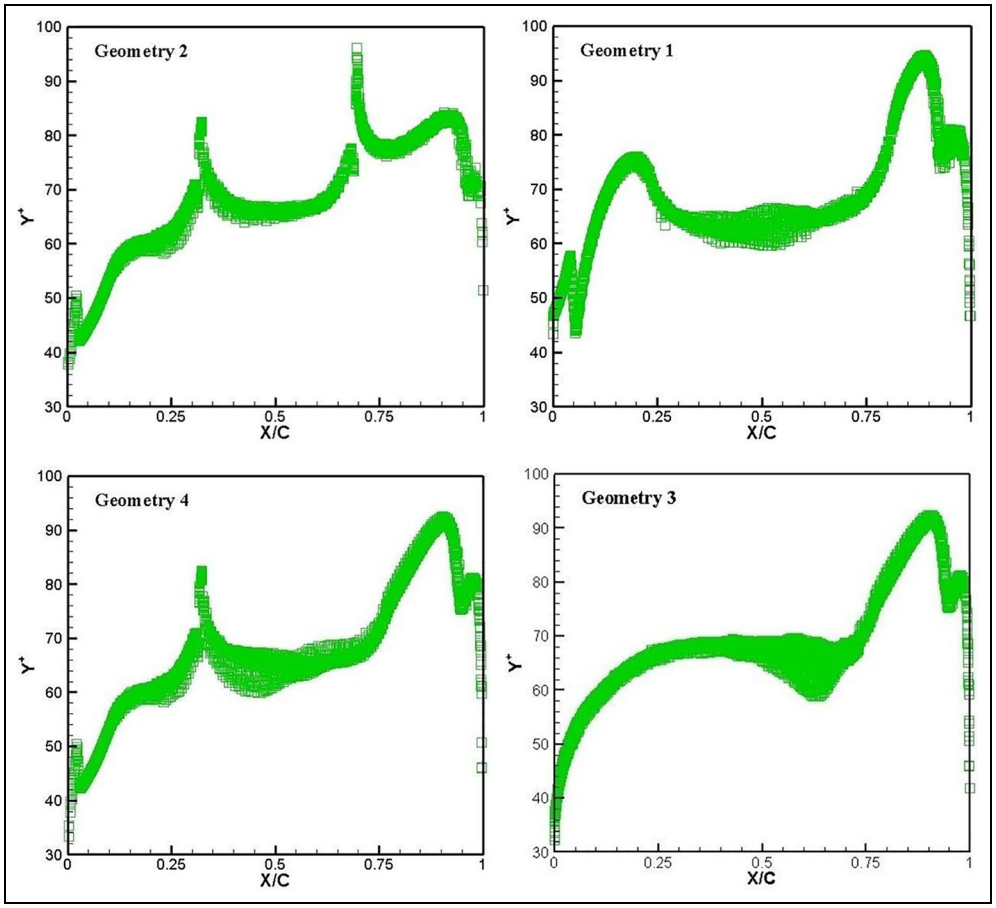

Figure 15. y^+ for different geometries.

Table 3. Comparison of the drag and lift force for different geometries.

Geometry	Drag coefficient $(\times 10)^{-2}$	Lift coefficient	Drag force (N)	Percentage difference in drag force between Alam et al.'s results and present results
1	9.8525	1.1685	9.87022	2.12%
2	8.1355	0.84489	7.991653	17.28%
3	8.3342	0.93882	8.18561	15.27%
4	8.9705	1.0304	8.812825	8.78%

Figure 18 shows the wall shear contour on the body of the four designed AUV hulls. When the separation takes place, the wall shear becomes zero. As it is seen, the wall shear in tail of the geometries no. 1, no. 2, and no. 4 has reached to zero, therefore, indicating the separation of flow, while the wall shear in the tail of geometry no. 3, although tends toward 0, has not reached 0, thus, the particular tail shape used in geometry no. 3 (tail no. 3) has delayed the separation.

The velocity contour around different geometries is shown in Figure 19. According to the velocity counter, it is evident that the velocity in the stagnation point is 0. In addition, the favorable pressure gradient region in the front section of the hulls and the adverse pressure gradient at the rear of the hulls are high and low velocity, respectively. The blue region around the tail, which has a speed of 0, indicates the separation of the flow. As it is seen, this blue region is not seen the tail of geometry no. 3.

Figure 20 shows pressure contours around different AUV hulls. In the front section of the hulls, the stagnation point is visible. This point has the highest amount of pressure. With regard to the pressure contours, it is obvious that the stagnation point or the high-pressure region in the front section of the hulls of geometry no. 2 is less than that of the other geometries.

According to the results obtained from the analysis of the streamline plots, it is clear that the reversed flow has not occurred in the tail section of geometry no. 3. In addition, according to the velocity contour, it is

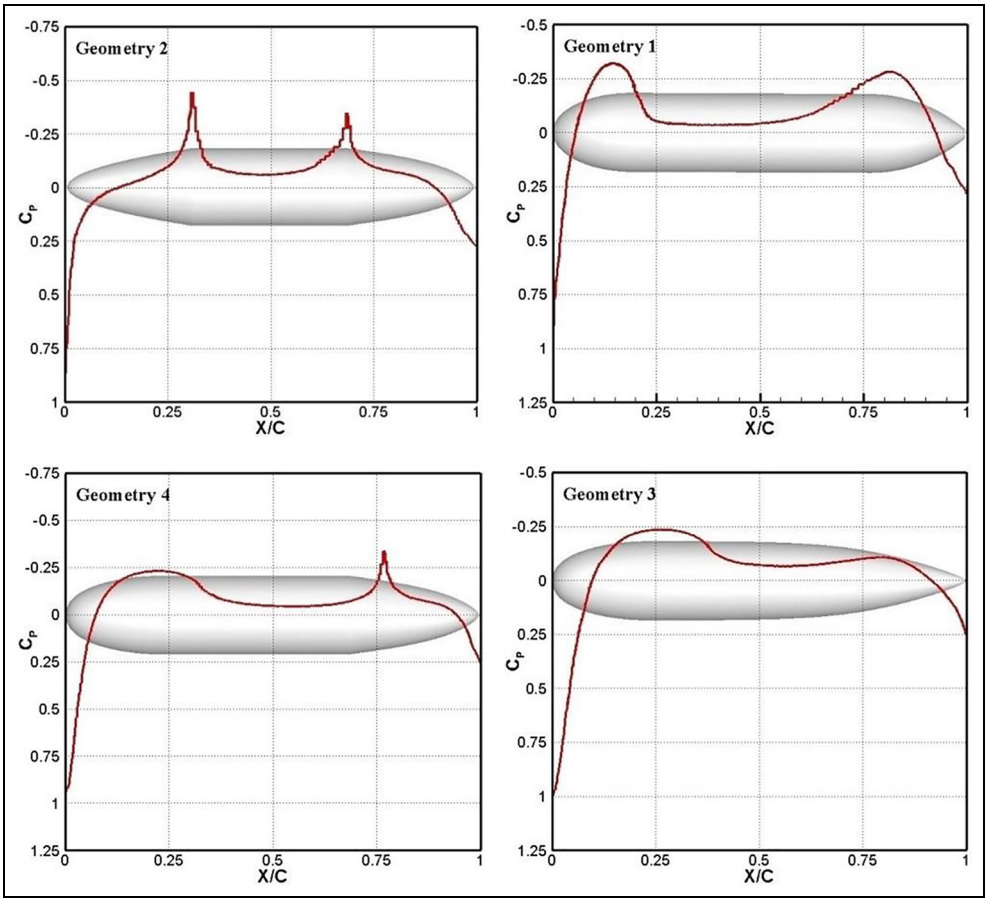

Figure 16. Pressure distribution around four geometries.

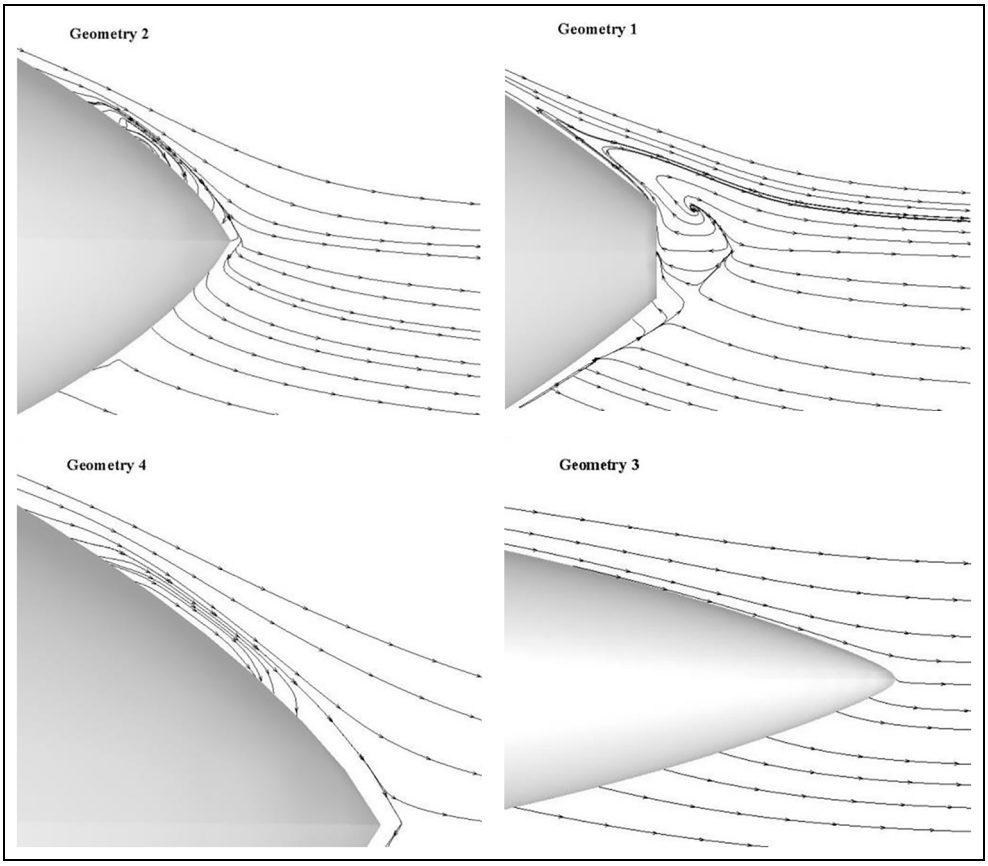

Figure 17. Streamlines plots around tails of different geometries.

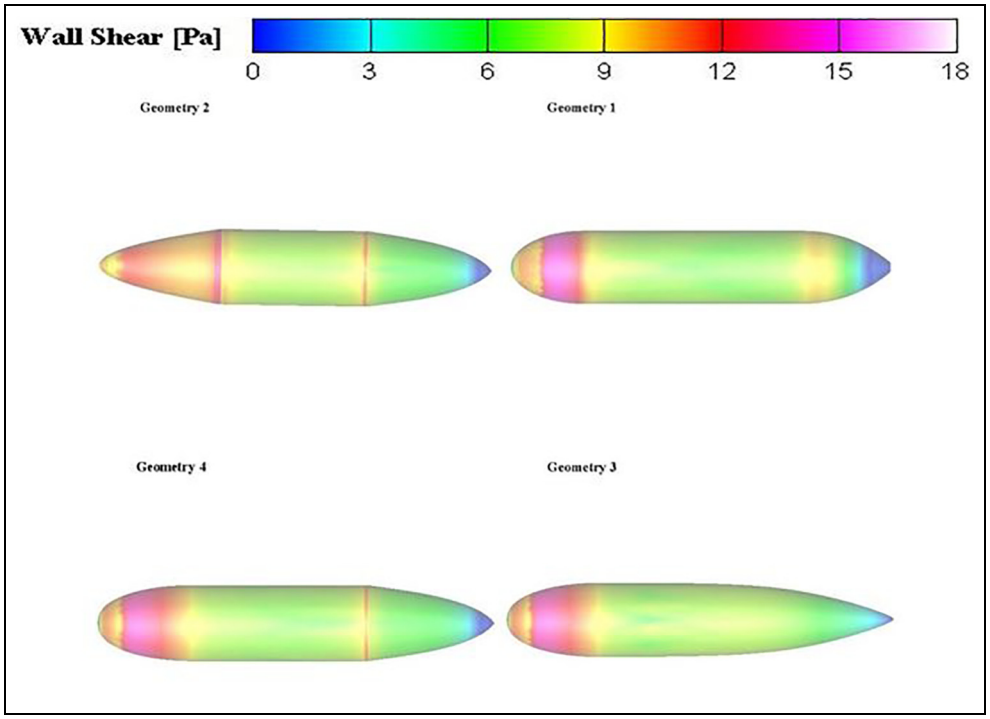

Figure 18. Wall shear contours of four geometries.

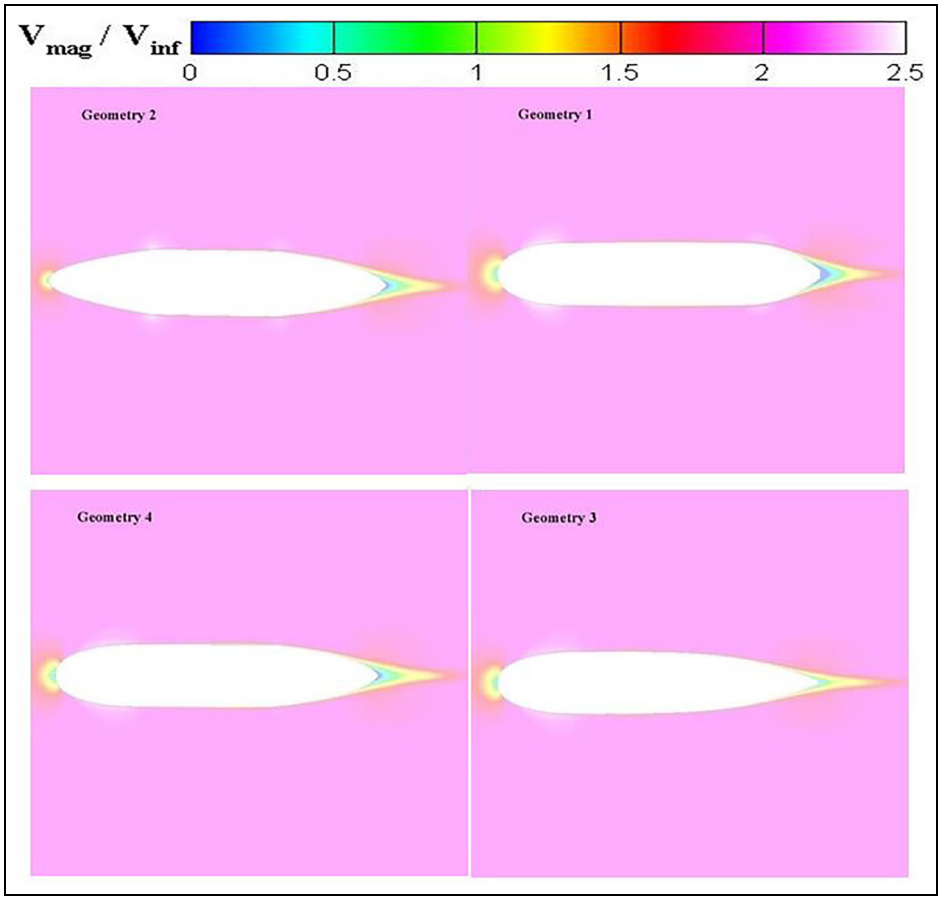

Figure 19. Velocity contours around different geometries.

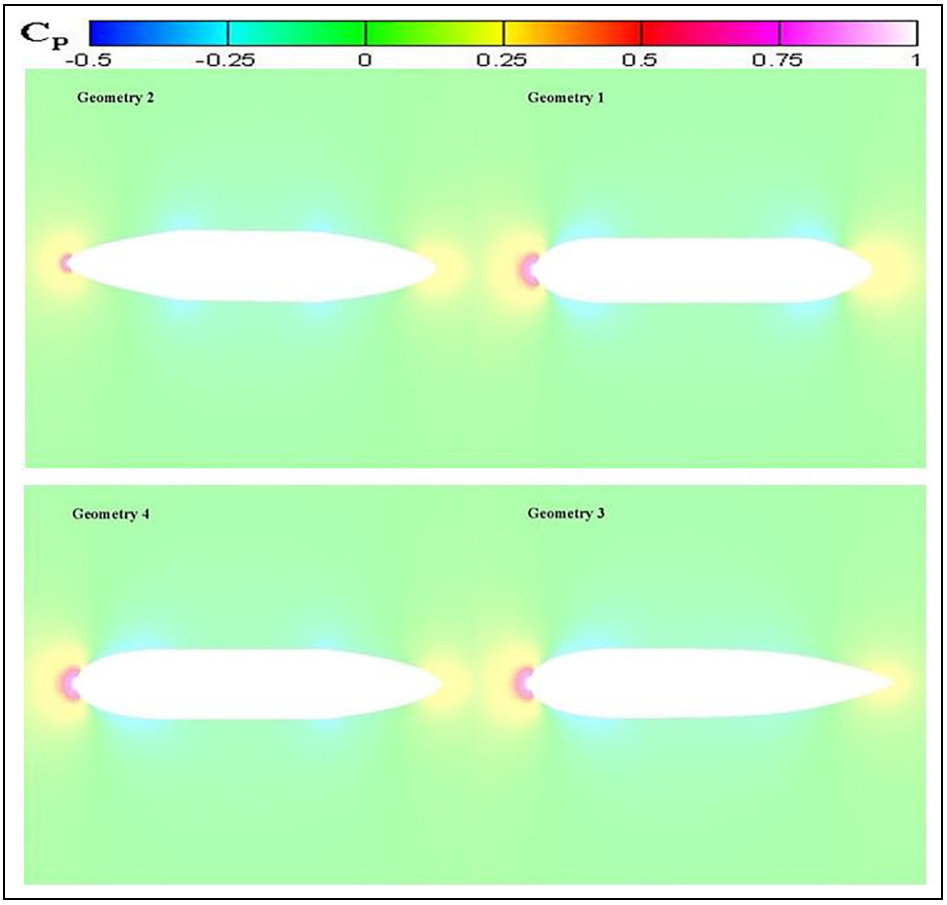

Figure 20. Pressure contours around different geometries.

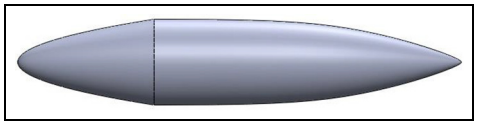

Figure 21. Geometry no. 5.

transparent that no zone with the speed of 0 has occurred at the rear section of geometry no. 3. Therefore, in accordance with the performed analyses, the tail of geometry no. 3 (tail no. 3) is the best tail. Moreover, according to the pressure contour, it is obvious that the best nose with the lowest static pressure belongs to geometry no. 2 (nose no. 3). Thus, to introduce the best shape, geometry no. 5 with tail and nose no. 3 is designed and examined. Geometry no. 5 is shown in Figure 21.

The numerical values obtained from the analysis of geometry no. 5 are the drag coefficient of $9.5609 \times 10,^{-4}$ the lift coefficient of 9.2998×10^{-3} and the drag force of 7.6349492 N, respectively.

Figure 22 illustrates the pressure coefficient, pressure contour, and velocity contour around geometry no. 5. Drag force in geometry no. 5 with a 26% decrease compared to the experimental results obtained by Alam et al. (Table (2)) and 4.5% reduction relative to the best geometry in terms of drag force (geometry no. 2) is better than the other geometries.

Conclusion

One of the ways to reduce energy consumption is to optimize the geometry of AUVs. Since the nose and tail are the most important parts of AUVs in hitting flows, in this research, numerical analysis of the flow around different AUV hulls with noses which are less than 400 mm in length inspired by Myring nose equations and parabolic curve equations of power series have been used. In addition, the design is based on those tails which are less than 500 mm in length derived from tangent ogive equation as well as the Myring equations. The total length of the AUV hulls is 1300 mm which have been investigated at a speed of 2 m/s and $\mathrm{Re} = 2.6 \times 10^6$ for better design of AUV hulls to reduce the drag force in water.

The results are obtained using the 3D steady flow to simulate the flow in the ANSYS Fluent software. In addition, k-ε Realizable model with enhanced wall treatment is used for solving the required problems. The numerical results of these analyses are compared with the numerical and experimental results carried out and they are shown an acceptable accuracy. The results

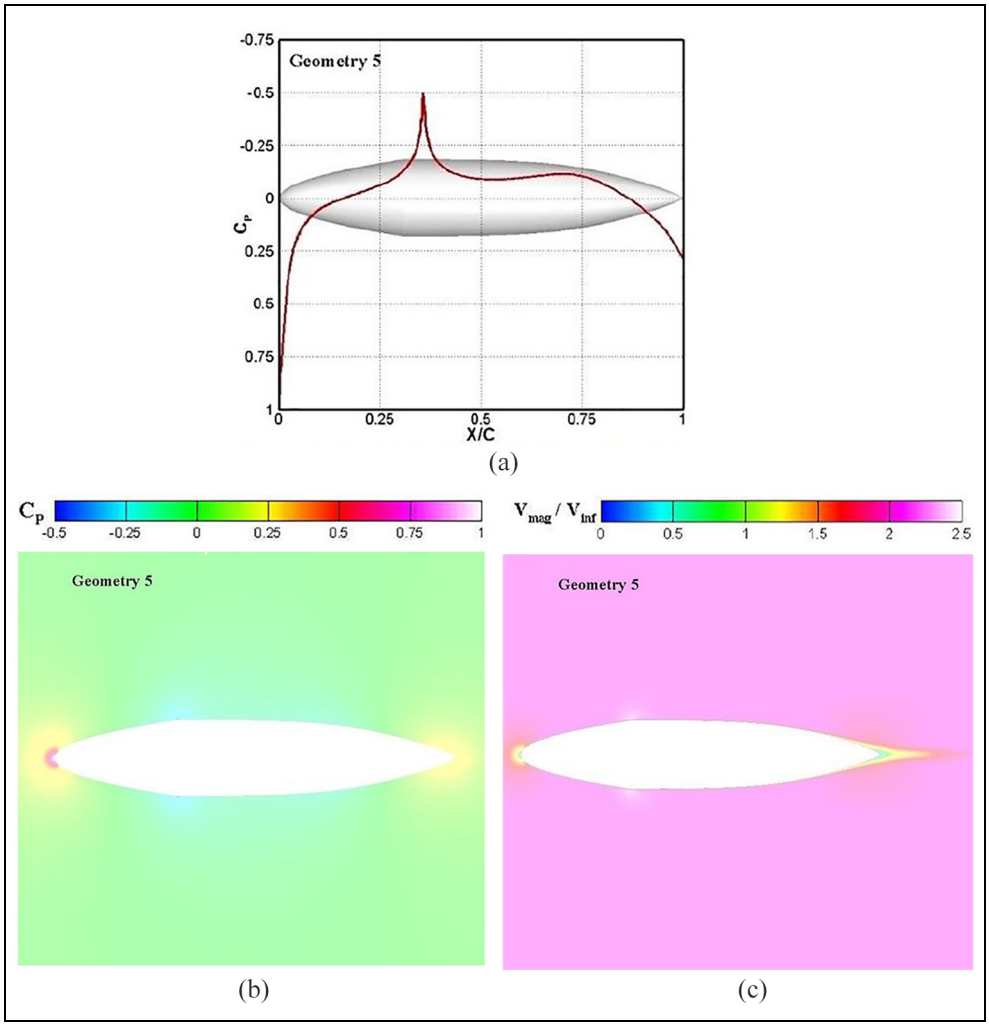

Figure 22. (a) Pressure distribution, (b) velocity contour, and (c) pressure contour around geometry no. 5.

of this study indicated that in all the designed geometries, the results are obtained using the 3D steady flow to simulate the flow in the ANSYS Fluent software. In addition, k-ε Realizable model with enhanced wall treatment is used for solving the required problems. The numerical results of these analyses are compared with the numerical and experimental results carried out, and they shown an acceptable accuracy. The results of this study indicated that in all the designed geometries except geometry no. 1, the drag force at an attack angle of 0° was less than that used in Alam et al.'s[26] studies.

In the four geometries examined, the least drag force is observed in geometries no. 2, no. 3, no. 4, and no. 1, respectively.

It is also found that the best conditions of speed and pressure are occurred at the nose of geometry no. 2 (nose no. 3) and tail of geometry no. 3 (tail no. 3). Therefore, to investigate the behavior of these geometries, a combination of the mentioned noses and tails have been designed in the form of geometry no. 5 and then it is thoroughly analyzed. After conducting the calculations, the obtained results show that geometry no. 5 with a drag force of 7.6349492 N has the least drag among all the other geometries and thus it is selected as the best geometry.

Declaration of conflicting interests

The author(s) declared no potential conflicts of interest with respect to the research, authorship, and/or publication of this article.

Funding

The author(s) received no financial support for the research, authorship, and/or publication of this article.

ORCID iD

Roham Lavimi https://orcid.org/0000-0002-4642-6336

References

1. Husaini M, Samad Z and Arshad MR. Autonomous underwater vehicle propeller simulation using computational fluid dynamic. *Computational Fluid Dynamics Technologies and* Applications, In Tech 2011; 293–314.
2. Husaini M, Samad Z and Arshad MR. CFD simulation of cooperative AUV motion. *Indian J Mar Sci* 2009; 38: 346–351.
3. Yamaguchi S, Kawanami T and Koterayama W. A study on shape optimization for an underwater vehicle based on numerical simulation. In: ISOPE Pacific / Asia offshore mechanics symposium, Daejeon, Korea, 2002, pp.17–20.
4. Song FX, Zhang LH, Wu ZL, et al. On resistance calculation for autonomous underwater vehicles. *Adv Mater Res* 2011; 189–193: 1745–1748.
5. Karim M, Rahman M, Mekanikal MA-J, et al. Numerical computation of viscous drag for axisymmetric underwater vehicles. *J Mekanikal* 2008; 26: 9–21.
6. Payne PR. Comment on "shaping of axisymmetric bodies for minimum drag in incompressible flow." *J Hydronautics* 1975; 9: 127–128.
7. Tang S, Ura T, Nakatani T, et al. Estimation of the hydrodynamic coefficients of the complex-shaped autonomous underwater vehicle TUNA-SAND. *J Mar Sc* 2009; 14: 373–386.
8. Sarkar T, Sayer PG and Fraser SM. Flow simulation past axisymmetric bodies using four different turbulence models. *Appl Math Model* 1997; 21: 783–792.
9. Shereena SG, Vengadesan S, Idichandyxs VG, et al. CFD study of drag reduction in axisymmetric underwater vehicles using air jets. *Eng Appl Comput Flu* 2013; 7: 193–209.
10. De Sousa JVN and de Macêdo ARL. Numerical analysis of turbulent fluid flow and drag coefficient for optimizing the AUV hull design. *Open J Fluid Dyn* 2014; 4: 263–277.
11. Joung TH, Sammut K, He F, et al. Shape optimization of an autonomous underwater vehicle with a ducted propeller using computational fluid dynamics analysis. *Int J Nav Archit Ocean Eng* 2012; 4: 44–56.
12. Gao T, Wang Y, Pang Y, et al. Hull shape optimization for autonomous underwater vehicles using CFD. *Eng Appl Comput Fluid Mech* 2016; 10: 599–607.
13. Nouri NM, Zeinali M and Jahangardy Y. AUV hull shape design based on desired pressure distribution. *J Mar Sci Technol* 2016; 21: 203–215.
14. Jagadeesh P, Murali K and Idichandy VG. Experimental investigation of hydrodynamic force coefficients over AUV hull form. *Ocean Eng* 2009; 36: 113–118.
15. Suman K, Rao D, Das H, et al. Hydrodynamic performance evaluation of an ellipsoidal nose for a high speed under water vehicle. *JJMIE* 2010; 4: 641–652.
16. Baker C. Estimating drag forces on submarine hulls, 2004, http://cradpdf.drdc-rddc.gc.ca/PDFS/unc35/p522579.pdf
17. Gomatam S, Vengadesan S and Bhattacharyya SK. Numerical simulations of flow past an autonomous underwater vehicle at various drift angles. *J Nav Archit Mar Eng* 2012; 9: 135–152.
18. Sarkar T, Sayer PG and Fraser SM. A study of autonomous underwater vehicle hull forms using computational fluid dynamics. *Int J Numer Methdos Fluids* 1997; 25: 1301–1313.
19. Saeidinezhad A, Dehghan AA and Dehghan Manshadi M. Nose shape effect on the visualized flow field around an axisymmetric body of revolution at incidence. *J Vis* 2014; 18: 83–93.
20. Saeidinezhad A, Dehghan AA and Dehghan Manshadi M. Experimental investigation of hydrodynamic characteristics of a submersible vehicle model with a non-axisymmetric nose in pitch maneuver. *Ocean Eng* 2015; 100: 26–34.
21. Dehghan AA, Saeidinezhad A and Dehghan Manshadi M. Effects of bulbous bow on cross-flow vortex structures around a streamlined submersible body at intermediate pitch maneuver: a numerical investigation. *J Mar Sci* 2016; 15: 8–15.
22. Saeidinezhad A, Dehghan AA and Dehghan Manshadi M. Boundary layer and surface pressure distributions behavior over a submarine nose model with two different nose shapes. *Sci Iran* 2019.
23. Zhang N, Shen HC and Yao HZ. Numerical simulation of cavity flow induced noise by les and FW-H acoustic analogy. *J Hydrodyn* 2010; 22: 242–247.
24. Liu H, Zhou B, Liu Z, et al. Numerical simulation of flow around a body of revolution with an appendage controlled by electromagnetic force. *Proc Inst Mech Eng G J Aerosp Eng* 2013; 227: 303–310.
25. Stevenson P, Furlong M and Dormer D. AUV shapes—combining the practical and hydrodynamic considerations. In: *Proceedings of the OCEANS*, Aberdeen, 17 September 2007, pp.1–6. New York: IEEE.
26. Alam K, Ray T and Anavatti SG. Design and construction of an autonomous underwater vehicle. *Neurocomputing* 2014; 142: 16–29.
27. *ANSYS Fluent, user manual*, version 15.0, 2015, http://www.pmt.usp.br/academic/martoran/notasmodelosgrad/ANSYS%20Fluent%20Users%20Guide.pdf
28. Myring DF. A theoretical study of body drag in subcritical axisymmetric flow. *Aeronaut Q* 1976; 27: 186–194.
29. Lavimi R, Hojaji M and Dehghan Manshadi M. Investigation of the aerodynamic performance and flow physics on cross sections of dragonfly wing on flapping and pitching motion in low Reynolds number. *Proc IMechE Part G: J Aerospace Engineering* 2019; 233: 589–603.